Spin-orbit photonics in a fixed cavity: Harnessing Bogoliubov modes of a Bose-Einstein condensate

Ghaisud Din, Muqaddar Abbas⋆ and Pei Zhang†

Ministry of Education Key Laboratory for Nonequilibrium Synthesis and Modulation
of Condensed Matter, Shaanxi Province Key Laboratory of Quantum Information
and Quantum Optoelectronic Devices, School of Physics,
Xi'an Jiaotong University, Xi'an 710049, China

⋆ muqaddarabbas@xjtu.edu.cn , † zhangpei@mail.ustc.edu.cn

Abstract

We present a theoretical investigation of spin-orbit photonics within a fixed mirror cavity system containing a Bose-Einstein condensate (BEC), in which the Bogoliubov excitation modes of the condensate are treated as effective mechanical oscillators. By embedding the condensate in a single-mode optical cavity, we explore the emergence and modulation of the photonic spin Hall effect (PSHE) through the spin-dependent transverse shifts of a weak probe field. The optical response –encoded in the real and imaginary components of the output field susceptibility– is systematically analyzed as a function of the condensate-cavity coupling strength, revealing a controllable enhancement or suppression of the spin-orbit interaction. Our model captures how the interplay between collective BEC excitations and cavity photon dynamics induces nontrivial modifications in spin-dependent light propagation. Notably, we uncover that the Bogoliubov mode coupling acts as a tunable channel for mediating spin angular momentum transfer within the cavity, offering a novel route for engineering compact, quantum-coherent spin-orbit photonic devices.

1 Introduction

The photonic spin Hall effect (PSHE) is a prominent manifestation of spin–orbit coupling (SOC) in optical systems, giving rise to a polarization-dependent lateral displacement of light at material interfaces [1]. This spatial splitting occurs due to the intrinsic interaction between the spin angular momentum of photons (associated with polarization) and their orbital trajectory, paralleling the spin Hall effect in electronic systems [2]. In such a photonic analogue, variations in the refractive index emulate the role of an electric field, producing a transverse shift that depends on the circular polarization components of the incident beam [1, 3, 4].

The theoretical basis for the PSHE was first established by Onoda *et al.* [1], with subsequent advancements contributed by Bliokh and co-authors, who offered a deeper understanding through conservation laws and geometric phase considerations [3]. Experimental verification was achieved in 2008 by Hosten and Kwiat via weak measurement protocols, enabling direct observation of the tiny polarization-induced beam shifts [5].

At its core, the PSHE arises from the conservation of total angular momentum in light–matter interactions, serving as a vital probe of spin–orbit phenomena in structured and inhomogeneous media [2, 6]. Techniques such as weak value amplification have proven highly effective in detecting the subtle spin-dependent displacements, significantly boosting the sensitivity of optical measurements [7, 8]. The broad utility of this effect has made it a cornerstone for numerous applications, ranging from precision metrology and quantum photonic devices to high-resolution optical imaging and sensor development [9–11].

Recent advancements in light–matter interaction have laid the foundation for the development of highly controllable quantum optical platforms, enabling precise manipulation of photonic and atomic degrees of freedom [12–15]. Within this context, Bose-Einstein condensate (BECs) have emerged as exemplary quantum many-body systems, exhibiting macroscopic coherence and distinct superfluid properties that set them apart from conventional phases of matter [16]. The experimental realization of BECs in ultracold dilute gases has catalyzed major progress in quantum optics and quantum simulation [17, 18], offering deep insights into quantum phase transitions, long-range coherence, and collective excitations [19–21].

The integration of BECs with high-finesse optical cavities has opened new frontiers for investigating hybrid quantum systems, where the collective motion of ultracold atoms strongly couples to quantized cavity modes [22, 23]. These platforms allow the exploration of self-organized phases [24], cavity-mediated superradiance [25], and nontrivial optical nonlinearities in the few-photon regime [26]. Notably, the condensate's low-energy excitation spectrum—particularly the Bogoliubov modes—exhibits behavior analogous to mechanical oscillators [27–29]. These quasi-particle excitations, being sensitive to cavity field fluctuations, introduce a new optomechanical degree of freedom that is both tunable and coherent. In cavity–BEC platforms, the coupling between the quantized cavity field and Bogoliubov excitations maps onto an effective optomechanical interaction, as established in theory and reviewed in Ref. [22]. Seminal experiments by the Esslinger group confirmed this paradigm, revealing cavity-enhanced backaction and many-body dynamics [16, 24].

Consequently, the BEC can be viewed not only as a quantum fluid but also as a dynamic mechanical element in cavity optomechanics. This dual nature enables light-induced manip-

ulation of condensate excitations and reciprocal modulation of the intracavity field. The bidirectional coupling between the BEC and the photonic field has been corroborated by theoretical and experimental investigations, revealing significant modifications to the system's optical susceptibility and quantum noise characteristics [16,30]. In this work, we harness these properties to study spin-orbit photonic phenomena—specifically, the PSHE—within a static cavity-BEC system, wherein Bogoliubov modes serve as mechanically active channels for mediating spin-dependent light propagation.

In this work, we theoretically investigate a hybrid cavity quantum electrodynamics system in which a BEC, confined within a fixed-mirror optical cavity, serves as an effective mechanical oscillator via its Bogoliubov excitation modes. Our focus lies in exploring how the spin–orbit interaction of light, manifested through the PSHE, is influenced by the dynamical coupling between the quantized intracavity field and the collective modes of the condensate. By analyzing the real and imaginary parts of the output probe field susceptibility, we characterize the spin-dependent light shifts induced by this coupling and elucidate the conditions under which spin-orbit photonic effects can be enhanced or suppressed. The role of the effective optomechanical interaction strength is examined in detail, revealing its impact on the PSHE signature. This study provides new insight into the coherent control of spin–orbit photonic phenomena using quantum fluids of light and matter, offering potential avenues for the realization of tunable, compact spin-sensitive photonic devices based on atomic condensates.

2 Theoretical model and physical configuration

We consider a hybrid optical system consisting of a BEC of N ultracold ^{87}Rb atoms confined inside an optical resonator, as shown in Fig. 1. A weak probe laser field, incident at an angle θ_{inc} on the partially reflective mirror M_1, interrogates the system. The probe beam has both transverse electric (TE) and transverse magnetic (TM) polarization components, with frequency ω_P and power P_P. The electric field amplitude is given by $|E_P| = \sqrt{\frac{2\kappa P_P}{\hbar\omega_P}}$, where κ denotes the cavity decay rate. Additionally, the cavity is coherently driven by a pump laser of frequency ω_L and power P_L, with amplitude $|E_L| = \sqrt{\frac{2\kappa P_L}{\hbar\omega_L}}$. In all simulations, we consider a normally incident pump with zero-degree polarization angle.

Upon reflection, the orthogonal circular polarization components of the probe field undergo a spatial separation transverse to the plane of incidence, indicative of the PSHE, as illustrated in Fig. 1. To make the manuscript self-contained, we first summarize the physical picture of the photonic spin Hall effect and how it connects to our transfer–matrix model and to the BEC-induced susceptibility.

2.1 Photonic spin Hall effect: Physical picture and working formulae

The PSHE in reflection originates from a spin–orbit interaction of light: the complex Fresnel coefficients $R_s(\theta, \epsilon_i)$ and $R_p(\theta, \epsilon_i)$ impart different amplitudes and phases to the TE and TM components that make up a linearly polarized input. In the circular basis $\mathbf{e}_\pm = (\mathbf{e}_{\text{TE}} \pm i\,\mathbf{e}_{\text{TM}})/\sqrt{2}$, this imbalance produces opposite, small centroid shifts for the $\sigma^\pm$ components at nonzero incidence angle θ_{inc}. The effect is most transparently controlled by the ratio R_s/R_p and by the angular dispersion $\partial_{\theta_{\text{inc}}} \ln R_p$.

For a spatially localized Gaussian probe beam, the electric field amplitudes of the reflected left- and right-handed circularly polarized components are:

$$\mathcal{E}_r^\pm(x_r, y_r, z_r) = \frac{\omega_0}{\omega} \exp\left[-\frac{x_r^2 + y_r^2}{\omega}\right]\left[R_p - \frac{2ix_r}{k\omega}\frac{\partial R_p}{\partial\theta} \mp \frac{2y_r\cot\theta}{k\omega}(R_s + R_p)\right]. \tag{1}$$

The transverse spatial shift of each spin component due to the PSHE is calculated as:

$$\delta_{p\pm} = \frac{\int y |\mathcal{E}_r^{\pm}(x_r, y_r, z_r)|^2 \, dx_r dy_r}{\int |\mathcal{E}_r^{\pm}(x_r, y_r, z_r)|^2 \, dx_r dy_r} . \tag{2}$$

Substituting Eq. (1) into Eq. (2) yields the spin-dependent displacement:

$$\delta_{p\pm} = \mp \frac{k_1 \omega_0^2 \, \mathrm{Re}\left[1 + \frac{R_s}{R_p} \right] \cot\theta_i}{k_1^2 \omega_0^2 + \left| \frac{\partial \ln R_p}{\partial \theta_i} \right|^2 + \left| \left(1 + \frac{R_s}{R_p} \right) \cot\theta_i \right|^2} . \tag{3}$$

The shift δ_{p+} and δ_{p-} represent the left- and right-circular polarization, respectively, with equal magnitude but opposite direction due to symmetry.

Equation (3) shows explicitly how the PSHE scales with the Fresnel ratio R_s/R_p and the angular derivative $\partial_{\theta_i} \ln R_p$. In our platform, both are tunable because $R_{s,p}$ depend on the intracavity permittivity $\epsilon_2 = 1 + \chi$, which is shaped by the BEC (Sec. 3).

2.2 Physical configuration (geometry and conventions)

We next state the optical geometry and modeling conventions used throughout. The probe $(\omega_{\mathrm{P}}, P_{\mathrm{P}})$ impinges on M_1 at θ_{inc} and is decomposed into TE (s) and TM (p) components relative to the plane of incidence; left/right circular components are defined by $\mathbf{e}_{\pm} = (\mathbf{e}_{\mathrm{TE}} \pm i\, \mathbf{e}_{\mathrm{TM}})/\sqrt{2}$. The pump $(\omega_{\mathrm{L}}, P_{\mathrm{L}})$ drives the cavity mode coherently. We employ the standard transfer–matrix formalism to derive the electromagnetic response of the cavity.

To model this interaction, we use the transfer matrix formalism for the ith layer of the three-layer system [31, 32]:

$$\mathcal{M}_i(k_x, \omega_p, d_i) = \begin{pmatrix} \cos(k_z^i) & \frac{i \sin(k_z^i)}{q_{is}} \\ i q_{is} \sin(k_z^i) & \cos(k_z^i) \end{pmatrix}, \tag{4}$$

where $k_z^i = d_i \sqrt{\epsilon_i k^2 - k^2 \sin^2\theta}$ is the longitudinal wave vector component in the ith layer of thickness d_i, and $q_{is} = \sqrt{\epsilon_i k^2 - k^2 \sin^2\theta}$ characterizes the TE polarization. The permittivity of the intracavity BEC medium, ϵ_2, is crucial in determining the shift, where $\epsilon_2 = 1 + \chi$ and χ is the effective susceptibility. To compute χ, we use the quantum Langevin formalism and input-output theory [33], with χ proportional to the steady-state output field amplitude, i.e., $\chi = E_{\mathrm{T}}$. In the next section, we derive the susceptibility by solving the coupled quantum equations of motion for the intracavity medium system dynamics.

The complete transfer matrix for the multilayer system is given by:

$$y(k_x, \omega_p) = \mathcal{M}_{1s}(k_x, \omega_p, d_1)\, \mathcal{M}_{2s}(k_x, \omega_p, d_2)\, \mathcal{M}_{3s}(k_x, \omega_p, d_3). \tag{5}$$

Based on the total transfer matrix formalism given in Eq.(5), the TE-polarized reflection coefficient of the probe field is given by

$$R_s = \frac{q_{1s}(y_{11} + y_{12} q_{3s}) - (q_{3s} y_{22} + y_{21})}{q_{1s}(y_{11} + y_{12} q_{3s}) + (q_{3s} y_{22} + y_{21})} . \tag{6}$$

Similarly, the TM-polarized reflection coefficient of the probe field is obtained by replacing q_{is} with p_{im}, and is given by

$$R_p = \frac{p_{1m}(y_{11} + y_{12} p_{3m}) - (p_{3m} y_{22} + y_{21})}{p_{1m}(y_{11} + y_{12} p_{3m}) + (p_{3m} y_{22} + y_{21})} , \tag{7}$$

where $p_{im} = \frac{q_{is}}{\epsilon_i}$ corresponds to the TM counterpart of the transverse wave vector in the ith layer. Note that $y(k_x, \omega_p)$ in Eq. (5) denotes the total transfer matrix and y_{mn} in Eqs. (6)–(7) correspond to its (m, n) element for the TE and TM polarizations, respectively. Once the susceptibility χ has been evaluated, the reflection coefficients R_s and R_p follow directly from the above equations in combination with the transfer-matrix relations.

2.3 From susceptibility to Fresnel coefficients and PSHE

The BEC modifies the intracavity response through $\epsilon_2(\omega) = 1 + \chi(\omega)$, which enters the layer matrix $\mathcal{M}_2$ in Eq. (4) and hence the total matrix y in Eq. (5). Consequently, R_s and R_p in Eqs. (6)–(7) become explicit functionals of $\chi(\omega)$ (and of the pump/probe conditions). Because the PSHE shift $\delta_{p\pm}$ [Eq. (3)] depends on the ratio R_s/R_p and on $\partial_{\theta_i} \ln R_p$, tuning the BEC–cavity parameters provides a coherent, *in situ* handle to control the magnitude and sign of the spin-dependent displacement.

2.4 Perspective and novelty

Conventional PSHE platforms (planar interfaces, metasurfaces, weak-measurement schemes) are typically passive. In contrast, our cavity–BEC architecture offers a *coherently tunable* route to PSHE: the Bogoliubov-mode–mediated susceptibility χ reshapes ϵ_2, thereby engineering $R_{s,p}$ and the angular dispersion that enter Eq. (3). This coupling enables operating regimes and dynamical control (via pump/probe settings and BEC–cavity parameters) that are not accessible in passive optics, providing a clear perspective on the novelty of our approach.

Assumptions and validity. Our analysis uses the paraxial, small-displacement approximation for a Gaussian probe; material dispersion is captured by $\chi(\omega)$ derived in Sec. 3. Under the parameters considered, higher-order spatial and nonparaxial corrections are negligible.

Table 1: Symbols and parameters used. Nominal values match those used in the simulations (see figure captions).

Symbol	Meaning	Notes/Units
ω_m	Bogoliubov mode frequency	$2\pi \times 15.2$kHz
κ	Cavity intensity decay rate	$0.05\omega_m$
ω_0	Probe waist at reflection plane	50λ
λ	wavelength	780 nm
$\chi = E_T$	Intracavity susceptibility (Sec. 3)	complex
ϵ_2	Intracavity permittivity	$1 + \chi$
R_s, R_p	Fresnel reflection (TE/TM)	Eqs. (6)–(7)
q_{is}, p_{im}	TE/TM transverse factors	$p_{im} = q_{is}/\epsilon_i$
y_{mn}	Elements of total transfer matrix	Eq. (5)
$\delta_{p\pm}$	PSHE transverse shift	Eq. (3)
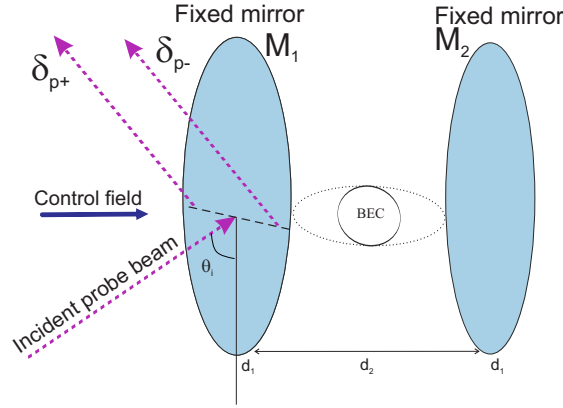
Figure 1: A schematic of the cavity setup comprises a Bose–Einstein condensate (BEC) of N ^{87}Rb atoms together with an optical parametric amplifier (OPA). Red arrows indicate the probe field entering and exiting through the left mirror M_1 at an incidence angle θ_{inc}. The pump field is applied at normal incidence with zero polarization angle (incident angle $= 0°$, polarization $= 0°$). δ_{p+} and δ_{p-} denote the transverse shifts of the reflected probe light corresponding to left- and right-circular polarizations, respectively. Both cavity mirrors, M_1 and M_2, are kept fixed.

3 System Hamiltonian and dynamics of a BEC-cavity coupled system

We examine a hybrid quantum setup consisting of a BEC coupled to a single–mode optical cavity. The system is governed by the total Hamiltonian:

$$
\begin{aligned}
\mathscr{H} = {}& \int \mathrm{d}x \, \Psi^\dagger(x) \left[-\frac{\hbar^2}{2m}\frac{\mathrm{d}^2}{\mathrm{d}x^2} + V_{\text{ext}}(x) + \hbar U_0 \cos^2(kx) \, a^\dagger a \right] \Psi(x) \\
& + \hbar \omega_a \, a^\dagger a + i\hbar E_L(a^\dagger e^{-i\omega_L t} - a \, e^{i\omega_L t}) + i\hbar E_P(a^\dagger e^{-i\omega_P t} - a \, e^{i\omega_P t}).
\end{aligned}
\tag{8}
$$

Here, $\hat{\Psi}^\dagger(x)$ and $\hat{a}^\dagger$ denote the creation operators for the atomic field and the cavity photons, respectively. The cavity supports a standing–wave mode with spatial profile $\cos(kx)$, where the wave number is $k = 2\pi/\lambda$. The dispersive light shift is quantified by $U_0 = g_0^2/\Delta_a$, with g_0 the single–photon atom–cavity coupling and Δ_a the atom–cavity detuning. Coherent drives at angular frequencies ω_L and ω_P enter through the (complex) amplitudes E_L and E_P.

Moving into the rotating frame at ω_L and applying the Bogoliubov approximation for atomic excitations, the Hamiltonian simplifies to:

$$
\mathcal{H} = \hbar\Delta_a \, a^\dagger a + \hbar\omega_m \, b^\dagger b + \hbar g_{bc} \, a^\dagger a(b + b^\dagger) + i\hbar E_L(a^\dagger - a) + i\hbar E_P\left(a^\dagger e^{-i\delta t} - a e^{i\delta t}\right),
\tag{9}
$$

where $\Delta_a = \omega_a + \frac{U_0 N}{2} - \omega_L$ includes the mean-field shift from N atoms, $\omega_m = 4\omega_{\text{rec}}$ is the Bogoliubov mode frequency with $\omega_{\text{rec}} = \hbar k^2/2m$, and $g_{bc} = \frac{U_0}{2}\sqrt{N/2}$ represents the effective optomechanical coupling. The final two terms represent the interaction between the cavity and the external driving fields: the pump and probe lasers, characterized by a detuning $\delta = \omega_P - \omega_L$ between the pump and probe frequencies.

Including dissipation and the accompanying quantum fluctuations, the dynamics of the cavity and mechanical modes are governed by the Heisenberg-Langevin equations:

$$
\dot{a} = -(i\Delta_a + \kappa)a - ig_{bc}\, a(b + b^\dagger) + E_L + E_P \, e^{-i\delta t} + \sqrt{2\kappa}\, a_{\text{in}},
\tag{10}
$$

$$
\dot{b} = -(i\omega_m + \gamma_m)\, b - ig_{bc}\, a^\dagger a + \sqrt{2\gamma_m}\, \xi,
\tag{11}
$$
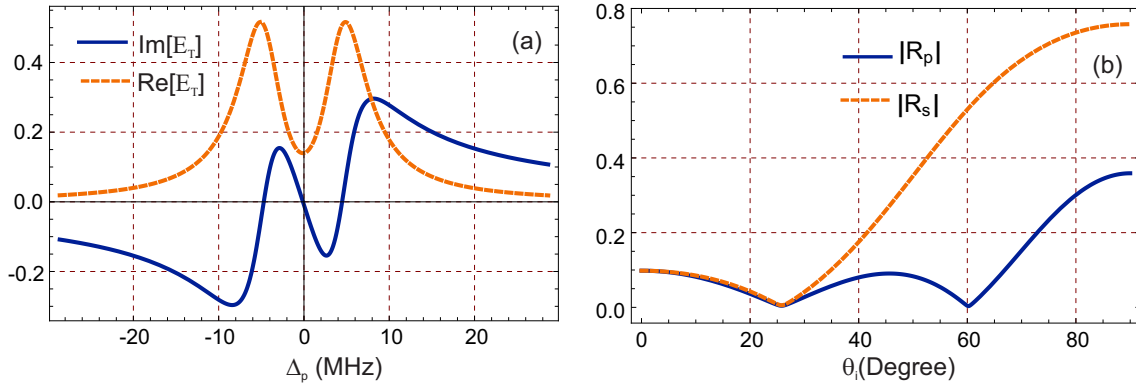
Figure 2: (a) Intracavity BEC response: dispersion (solid) and absorption (dashed) versus probe detuning Δ_p. Parameters: $\omega_m/2\pi = 15.2$ kHz, $\gamma_m/2\pi = 0.21$ kHz, $\omega_{rec}/2\pi = 3.8$ kHz, $\lambda = 780$ nm, $L = 1.25 \times 10^{-4}$ m, $G_{BC} = 0.05\,\omega_m$, and cavity decay $\kappa = 0.05\,\omega_m$. (b) Angular dependence of the Fresnel reflection magnitudes $|R_s|$ and $|R_p|$ as functions of the incidence angle θ_i, evaluated at resonant detuning $\Delta_p = 0$. The remaining parameters are $\epsilon_0 = 1$, $\epsilon_1 = \epsilon_3 = 2.22$, $\epsilon_2 = 1 + E_T$, mirror thicknesses $d_1 = 0.1 \times 10^{-6}$ m and $d_2 = 0.4 \times 10^{-6}$ m.

where κ and γ_m denote the damping rates of the cavity and the mechanical resonator, respectively, and $\hat{a}_{in}$ and $\hat{\xi}$ are the corresponding input–noise operators.

Expanding around steady-state values $a = \alpha + \delta a$, $b = \beta + \delta b$, and retaining only first-order fluctuations yields:

$$\delta\dot{a} = -(i\Delta + \kappa)\,\delta a - iG_{BC}(\delta b + \delta b^\dagger) + E_P\,e^{-i\delta t}\,, \tag{12}$$

$$\delta\dot{b} = -(i\omega_m + \gamma_m)\,\delta b - iG_{BC}\,\delta a^\dagger - iG_{BC}^*\,\delta a\,, \tag{13}$$

with $G_{BC} = g_{bc}|\alpha|$ and $\Delta = \Delta_a - g_{bc}(\beta + \beta^*)$ is the effective detuning.

The steady-state intracavity amplitudes are given by:

$$\alpha = \frac{E_L(\kappa - i\Delta)}{\kappa^2 + \Delta^2}\,, \tag{14}$$

$$\beta = -\frac{ig_{bc}|\alpha|^2}{i\omega_m + \gamma_m}\,. \tag{15}$$

To study the probe response, we adopt the ansatz:

$$\delta a(t) = \delta a_- e^{-i\delta t} + \delta a_+ e^{i\delta t}\,, \tag{16}$$

$$\delta b(t) = \delta b_- e^{-i\delta t} + \delta b_+ e^{i\delta t}\,. \tag{17}$$

Substituting into Eqs. (12)–(13) and solving algebraically, the total cavity output field reads:

$$E_{out}(t) + E_P e^{-i\delta t} + E_L = \sqrt{2\kappa}\,a(t)\,, \tag{18}$$

where the output probe signal is decomposed as:

$$E_{out}(t) = E_{out}^{(0)} + E_{out}^{(+)} E_P e^{-i\delta t} + E_{out}^{(-)} E_P e^{i\delta t}\,. \tag{19}$$

The probe transmission is then characterized by:

$$E_{out}^{(+)} = \frac{\sqrt{2\kappa}\,a_-}{E_P} - 1\,, \tag{20}$$

$$E_T = \frac{\sqrt{2\kappa}\,a_-}{E_P}\,, \tag{21}$$

where a_- is the intracavity response to the probe field, obtained as:

$$a_- = \frac{\mathcal{A}}{\mathcal{B}}, \tag{22}$$

with:

$$\mathcal{A} = E_P\Big[2i G_{BC}^2 \omega_m + (\gamma_m - i\Delta_p)\big(\gamma_m - i(\Delta_p + 2\omega_m)\big)\big(\kappa - i(\Delta_p + 2\omega_m)\big)\Big], \tag{23}$$

$$\mathcal{B} = -(\kappa - i\Delta_p)\Big[-2i G_{BC}^2 \omega_m + (\gamma_m - i\Delta_p)\big(i\gamma_m + \Delta_p + 2\omega_m\big)\big(i\kappa + \Delta_p + 2\omega_m\big)\Big]$$
$$+ 2G_{BC}^2 \big(-i\kappa - \Delta_p - 2\omega_m\big)\omega_m. \tag{24}$$

In the resolved sideband regime, where $\omega_m \gg \kappa$ and the effective detuning is set to $\Delta = \omega_m$, the term $\Delta_p = \delta - \omega_m$ in the previous expression corresponds to the effective probe detuning reduced by the mechanical Bogoliubov mode frequency ω_m, i.e., $\Delta_p = \delta - \omega_m$. The transmission of the probe E_T effectively serves as the susceptibility χ of the intra-cavity medium, that is, $\chi = \chi_r + i\chi_i \equiv E_T$. Both real and imaginary parts of χ determine the phase and absorption response of the system, respectively, and can be accessed via homodyne detection techniques. Spontaneous emission is neglected due to the large atom-cavity detuning, we assume a single linear polarization of the cavity field and consider a scalar (single–component) BEC. The damping rate of the Bogoliubov mechanical mode is introduced phenomenologically to account for residual decay of the collective excitation, and inter-atomic collisions are neglected in the weakly interacting regime.

4 Results and discussion

Unless stated otherwise, we adopt experimentally realistic parameters [34, 35]: $\omega_m/2\pi = 15.2\,$kHz, $\gamma_m/2\pi = 0.21\,$kHz, $\omega_{rec}/2\pi = 3.8\,$kHz, $\lambda = 780\,$nm, and $L = 1.25 \times 10^{-4}\,$m. For the PSHE analysis we further set $\epsilon_0 = 1$, $\epsilon_1 = \epsilon_3 = 2.22$, with mirror-layer thicknesses $d_1 = 0.2\,\mu$m and $d_2 = 5\,\mu$m.

We operate in the far–off–resonant (dispersive) regime, so that spontaneous emission is negligible and the electronically excited states can be adiabatically eliminated. The analysis is restricted to a single, linearly polarized cavity mode aligned with the x–axis. The associated magnetic field is treated implicitly and does not alter the strictly one–dimensional optomechanical motion. Ultracold atom–atom collisions are included at the mean–field level, leading to a renormalization of the effective mechanical frequency; this shift is absorbed into the parameter set used in our simulations.

Only a single internal state of the BEC is considered, since other hyperfine states are far-detuned and remain negligibly populated. The mechanical mode is further characterized by a damping rate γ_m, which accounts for decoherence arising from atomic collisions as well as residual coupling to the thermal environment.

Figure 2 summarizes the optical response of the BEC–cavity platform. In panel (a) we display the dispersive part (solid; Re χ) and the absorptive part (dashed; Im χ) as functions of the probe detuning Δ_p. The curves are computed with experimentally accessible parameters: $\omega_m/2\pi = 15.2$ kHz, $\gamma_m/2\pi = 0.21$ kHz, $\omega_{rec}/2\pi = 3.8$ kHz, and a cavity length $L = 1.25 \times 10^{-4}$ m. The light–matter coupling and cavity loss are set to $G_{BC} = 0.05\,\omega_m$ and $\kappa = 0.05\,\omega_m$, respectively.

The dispersion curve exhibits a steep slope in the vicinity of $\Delta_p = 0$, signifying strong group velocity dispersion indicative of slow-light effects. This region corresponds to a rapid variation of the refractive index, a consequence of coherent interference within the hybrid cavity–BEC system. Meanwhile, the absorption profile displays a pronounced transparency window near

resonance, suggesting the presence of an electromagnetically induced transparency (EIT)-like phenomenon. This feature stems from destructive interference between competing excitation pathways in the coupled light-matter system, which precisely suppresses absorption at resonance.

In panel (b), we analyze the angular dependence of the Fresnel reflection magnitudes $|R_s|$ and $|R_p|$ at resonant probe detuning $\Delta_p = 0$. The dielectric environment comprises layers with permittivities $\epsilon_0 = 1$, $\epsilon_1 = \epsilon_3 = 2.22$, and $\epsilon_2 = 1 + E_T$, where E_T represents a tunable external control parameter. The multilayer stack includes mirror thicknesses $d_1 = 0.1 \times 10^{-6}$ m and $d_2 = 0.4 \times 10^{-6}$ m.

The results show that $|R_p|$ displays a dip around the Brewster angle, a classical effect arising from zero reflectivity for p-polarized light at a specific angle of incidence. In contrast, $|R_s|$ remains finite and comparatively flat across the angular spectrum, reflecting its insensitivity to such Brewster-angle effects. The sharp angular contrast between the two polarizations establishes a favorable condition for spin-dependent optical phenomena, such as the photonic PSHE, where the angular separation of spin components is maximized.

These findings confirm that the system supports tunable dispersion and polarization-selective reflection, essential for tailoring light propagation, enhancing light–matter interactions, and enabling spin-dependent optical control. The tunability via Δ_p and θ_i, along with the engineered dielectric environment, underscores the potential of this platform for applications in slow-light devices, precision sensing, and spin-resolved photonic interfaces.
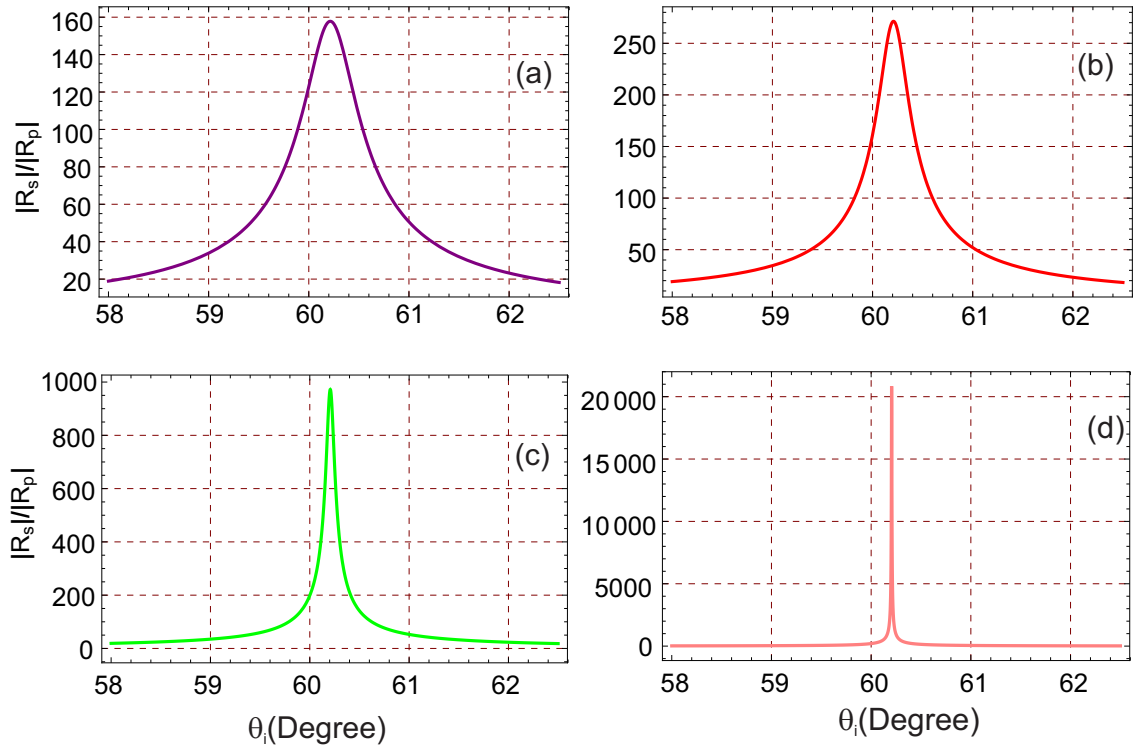
Figure 3: The amplitude ratio $|R_s|/|R_p|$ is shown as a function of the incidence angle θ_i for four probe detunings: (a) $\Delta_p = 0$, (b) $\Delta_p = -0.05\,\omega_m$, (c) $\Delta_p = -0.10\,\omega_m$, and (d) $\Delta_p = -0.12\,\omega_m$. Unless specified otherwise, the parameters are $\omega_m/2\pi = 15.2$ kHz, $\gamma_m/2\pi = 0.21$ kHz, $\omega_{rec}/2\pi = 3.8$ kHz, $\lambda = 780$ nm, $L = 1.25 \times 10^{-4}$ m, $G_{BC} = 0.05\,\omega_m$, $\kappa = 0.05\,\omega_m$, $\epsilon_0 = 1$, $\epsilon_1 = \epsilon_3 = 2.22$, $\epsilon_2 = 1 + E_T$, with mirror-layer thicknesses $d_1 = 0.1\,\mu$m and $d_2 = 0.4\,\mu$m.
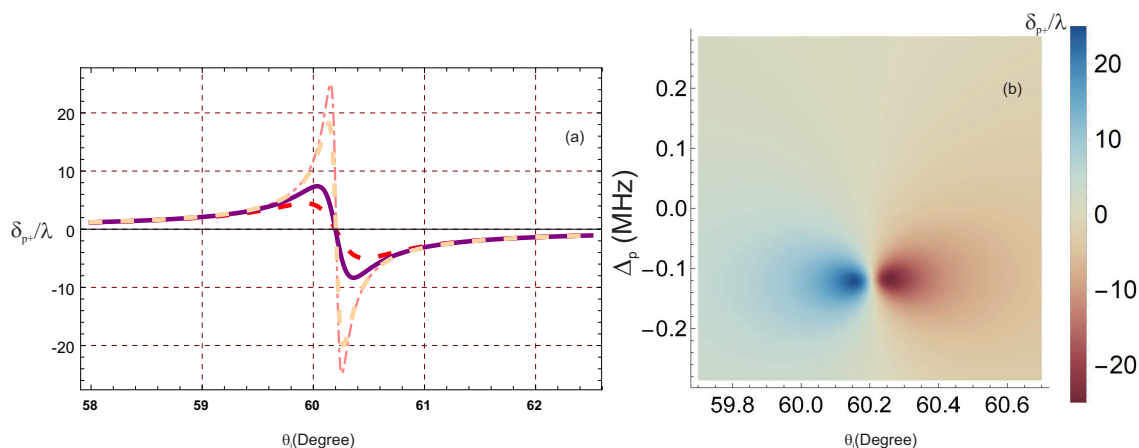
Figure 4: (a) Normalized PSHE displacement δ_{p+}/λ versus incidence angle θ_i for four probe detunings: $\Delta_p = 0$ (red, dashed), $\Delta_p = -0.05\,\omega_{\mathrm{m}}$ (purple, solid), $\Delta_p = -0.10\,\omega_{\mathrm{m}}$ (light gray, dashed), and $\Delta_p = -0.12\,\omega_{\mathrm{m}}$ (pink, dash–dot). (b) Density map of δ_{p+}/λ in the (θ_i, Δ_p) plane. Unless stated otherwise, parameters are $\omega_{\mathrm{m}}/2\pi = 15.2$ kHz, $\gamma_{\mathrm{m}}/2\pi = 0.21$ kHz, $\omega_{\mathrm{rec}}/2\pi = 3.8$ kHz, $\lambda = 780$ nm, $L = 1.25\times10^{-4}$ m, $G_{\mathrm{BC}} = 0.05\,\omega_{\mathrm{m}}$, $\kappa = 0.05\,\omega_{\mathrm{m}}$, $\epsilon_0 = 1$, $\epsilon_1 = \epsilon_3 = 2.22$, $\epsilon_2 = 1 + E_T$, and mirror–layer thicknesses $d_1 = 0.1\,\mu$m, $d_2 = 0.4\,\mu$m.

To quantify the polarization sensitivity, we evaluate the ratio of reflection amplitudes $|R_s|/|R_p|$ for s– and p–polarized light as a function of the incidence angle θ_i for several probe detunings Δ_p (see Fig. 3). The calculations employ experimentally accessible values: $\omega_{\mathrm{m}}/2\pi = 15.2$ kHz, $\gamma_{\mathrm{m}}/2\pi = 0.21$ kHz, $\omega_{\mathrm{rec}}/2\pi = 3.8$ kHz, and $\lambda = 780$ nm. The optical cavity parameters are $L = 1.25 \times 10^{-4}$ m, $G_{\mathrm{BC}} = 0.05\,\omega_{\mathrm{m}}$, and $\kappa = 0.05\,\omega_{\mathrm{m}}$. The stratified dielectric is specified by $\epsilon_0 = 1$, $\epsilon_1 = \epsilon_3 = 2.22$, and $\epsilon_2 = 1 + E_T$, where E_T represents a tunable contribution set by an external control. The layer thicknesses are fixed at $d_1 = 0.1 \times 10^{-6}$ m and $d_2 = 0.4 \times 10^{-6}$ m.

Figure 3(a)–(d) correspond to detuning values $\Delta_p = 0$, $-0.05\omega_{\mathrm{m}}$, $-0.1\omega_{\mathrm{m}}$, and $-0.12\omega_{\mathrm{m}}$, respectively. For $\Delta_p = 0$, the ratio $|R_s|/|R_p|$ exhibits a moderate angular variation around $\theta_i \approx 60.2°$, which serves as the reference case where neither polarization component is preferentially enhanced or suppressed. As the detuning becomes increasingly negative, the angular profile of the ratio becomes noticeably asymmetric. Specifically, for $\Delta_p = -0.05\omega_{\mathrm{m}}$, the ratio increases rapidly for incident angles slightly below the reference value and decreases more gradually afterwards.

For larger detuning values, e.g. $\Delta_p = -0.10\omega_{\mathrm{m}}$ and $-0.12\omega_{\mathrm{m}}$, the maximum value of $|R_s|/|R_p|$ increases further, and the angular region where the enhancement occurs becomes narrower around the critical angle. This behavior is associated with the detuning–induced modification of the optical susceptibility, which enhances the coupling of the probe field to spin–polarized modes of the cavity–BEC hybrid system.

These results demonstrate that probe detuning provides a powerful control parameter for tailoring the polarization–dependent reflection. By tuning Δ_p, one can selectively enhance or suppress a given polarization component over a narrow angular range, which may be exploited for polarization–resolved optical filtering and sensing devices.

Figure 4 examines the behavior of the normalized PSHE shift, δ_{p+}/λ, as a function of the incident angle θ_i, with particular emphasis on the role of probe detuning Δ_p. Panel (a) shows four representative curves for different detuning values, while panel (b) displays a density map of δ_{p+}/λ in the (θ_i, Δ_p) plane.
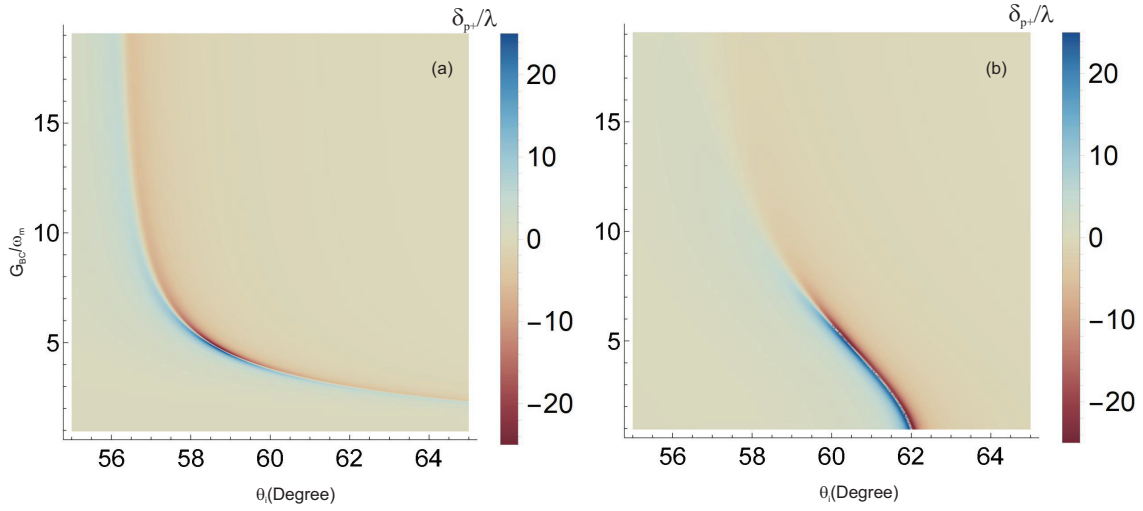
Figure 5: Density plot of the normalized PSHE shift, δ_{p+}/λ, as a function of the incident angle θ_i and the cavity–BEC coupling strength G_{BC}, for two dissipation regimes: (a) when the cavity dissipation rate κ equals the BEC dissipation rate γ_b, i.e., $\kappa/2\pi = \gamma_m/2\pi = 0.21$ kHz, and (b) when the cavity dissipation rate exceeds that of the BEC, i.e., $\kappa = 0.5\,\omega_m$ and $\gamma_m/2\pi = 0.21$ kHz. The remaining parameters are: probe detuning $\Delta_p = -0.12\,\omega_m$ (corresponding to the maximum PSHE), mechanical frequency $\omega_m/2\pi = 15.2$ kHz, recoil frequency $\omega_{rec}/2\pi = 3.8$ kHz, wavelength $\lambda = 780$ nm, cavity length $L = 1.25 \times 10^{-4}$ m, dielectric constants $\epsilon_0 = 1$, $\epsilon_1 = \epsilon_3 = 2.22$, $\epsilon_2 = 1 + E_T$, mirror thicknesses $d_1 = 0.1 \times 10^{-6}$ m and $d_2 = 0.4 \times 10^{-6}$ m.

In Fig. 4(a), the PSHE shift has a pronounced maximum at the critical incident angle $\theta_i \approx 60.2°$. The magnitude and the shape of this maximum are strongly influenced by the probe detuning. For $\Delta_p = 0$, the angular profile is almost symmetric. As the detuning is made negative, the magnitude of the peak increases and the profile becomes asymmetric, with a steeper increase on the low–angle side and a slower decay on the high–angle side. This evolution is a signature of the dispersive response of the optomechanical system, since detuning modifies the effective refractive index and the corresponding spin–orbit coupling strength.

Panel (b) illustrates how δ_{p+}/λ varies across a range of incident angles and detuning values. A distinct sign inversion occurs in the vicinity of the critical angle and zero detuning, highlighting the transition from negative to positive PSHE shift. The blue and red regions in the density plot correspond to opposite transverse shifts of the two circularly–polarized components, and their evolution with detuning reflects the interference between these components. The resulting dip–peak pattern indicates that the spin sensitivity is maximal close to the critical incident angle.

These findings show that the PSHE can be tuned efficiently by adjusting the probe detuning, providing a promising route towards spin–selective photonic devices, such as tunable polarization–dependent beam deflectors and quantum optical sensors.

Figure 5 displays density maps of the normalized PSHE shift δ_{p+}/λ as functions of the incidence angle θ_i and the BEC–cavity coupling G_{BC}, evaluated under two distinct dissipation conditions. These regimes are differentiated by the relative sizes of the cavity decay rate κ and the mechanical BEC damping γ_m. All panels are generated using experimentally realistic parameters specified in the caption.

In panel (a), the condition $\kappa/2\pi = \gamma_m/2\pi = 0.21$ kHz is considered, which signifies balanced dissipation rates for the cavity and the BEC. Under this symmetric dissipation regime, a pronounced peak in the PSHE shift appears around $\theta_i \approx 59°$, particularly for weak to moderate coupling strengths ($G_{BC}/\omega_m \lesssim 10$). This behavior is attributed to the resonant enhancement of the light–matter interaction, where the PSHE is maximized due to efficient momentum transfer at the interface. The sharp color gradient near this angular region also highlights a strong angular sensitivity of the shift, making the system favorable for precision sensing applications.

In contrast, panel (b) presents the scenario where the cavity dissipation dominates ($\kappa = 0.5\omega_m$, while $\gamma_m/2\pi = 0.21$ kHz remains fixed). In this case, the overall magnitude of the normalized PSHE shift increases compared to panel (a), with broader regions of significant positive values. The peak region shifts slightly to larger incident angles, and the PSHE becomes less sharply localized in both angle and coupling strength. The enhancement in this regime arises due to increased photonic leakage, which facilitates more efficient extraction of spin-dependent components of light, thus amplifying the observable PSHE. However, the trade-off is a reduction in the quality factor of the cavity, which could limit coherence in certain quantum applications.

The comparison between panels (a) and (b) emphasizes the critical role of cavity dissipation in tailoring the PSHE. Specifically, by engineering the relative magnitudes of κ and γ_m, one can modulate the strength and angular profile of the PSHE shift. This tunability is vital for designing reconfigurable photonic devices based on spin–orbit interaction, such as polarization-resolved sensors or optical switches.

Overall, the results confirm that optimal control of dissipation parameters and light–matter coupling enables precise manipulation of spin-dependent photonic transport, with potential applications in chiral quantum optics and topological photonics.

5 Conclusion

We have theoretically examined spin–orbit photonic phenomena in a fixed-mirror optical cavity system coupled to a BEC, where Bogoliubov excitation modes function as effective mechanical resonators. By embedding the BEC within a single-mode cavity, our model uncovers how spin-dependent light–matter interactions manifest as PSHE shifts of a weak probe beam, which are highly sensitive to system parameters.

The analysis reveals strong dispersive and absorptive responses around specific probe detunings, evidencing the role of the BEC–cavity interaction in modifying the system's optical transparency. The angular dependence of the Fresnel coefficients further supports the emergence of spin-selective scattering near the Brewster angle, establishing the angle-dependent origin of the PSHE.

Through systematic exploration of the ratio $|R_s|/|R_p|$ and the corresponding PSHE shift δ_{p+}/λ, we demonstrate that the magnitude and sign of the transverse spin-dependent shift are strongly modulated by the probe field detuning. A critical enhancement of the PSHE occurs near resonance, highlighting the cavity-assisted control over the spin–orbit interaction channel. Additionally, the parameter regimes in which spin-orbit effects are maximized are clearly visualized through two-dimensional contour mappings.

Further insights establish how cavity dissipation governs the SHE response. In particular, under equal dissipation conditions for the cavity and the BEC ($\kappa = \gamma_m$), the shift profile becomes sharper and more localized, while higher cavity losses smooth out the transverse spin shift features. This illustrates the tunability of the spin–orbit effect via dissipative engineering.

Overall, our findings confirm that the interplay between Bogoliubov collective excitations and cavity photon dynamics not only mediates angular momentum exchange but also enables fine control over spin-dependent light steering. The BEC–cavity platform thus serves as a promising medium for developing reconfigurable, miniaturized spin–orbit photonic devices with potential applications in optical sensing, nonreciprocal signal processing, and quantum information routing.

Acknowledgments

Funding information This work was supported by the National Natural Science Foundation of China (Grant No. 12174301), the Natural Science Basic Research Program of Shaanxi (Program No. 2023-JC-JQ-01), and the Fundamental Research Funds for the Central Universities.

References

[1] M. Onoda, S. Murakami and N. Nagaosa, *Hall effect of light*, Phys. Rev. Lett. **93**, 083901 (2004), doi:10.1103/PhysRevLett.93.083901 [preprint doi:10.48550/arXiv.cond-mat/0405129].

[2] K. Y. Bliokh, F. J. Rodríguez-Fortuño, F. Nori and A. V. Zayats, *Spin-orbit interactions of light*, Nat. Photonics **9**, 796 (2015), doi:10.1038/nphoton.2015.201 [preprint doi:10.48550/arXiv.1505.02864].

[3] K. Y. Bliokh and Y. P. Bliokh, *Conservation of angular momentum, transverse shift, and spin Hall effect in reflection and refraction of an electromagnetic wave packet*, Phys. Rev. Lett. **96**, 073903 (2006), doi:10.1103/PhysRevLett.96.073903 [preprint doi:10.48550/arXiv.physics/0508093].

[4] J. Sinova, S. O. Valenzuela, J. Wunderlich, C. H. Back and T. Jungwirth, *Spin Hall effects*, Rev. Mod. Phys. **87**, 1213 (2015), doi:10.1103/RevModPhys.87.1213.

[5] O. Hosten and P. Kwiat, *Observation of the spin Hall effect of light via weak measurements*, Science **319**, 787 (2008), doi:10.1126/science.1152697.

[6] F. Cardano and L. Marrucci, *Spin-orbit photonics*, Nat. Photonics **9**, 776 (2015), doi:10.1038/nphoton.2015.232.

[7] L. Cai, M. Liu, S. Chen, Y. Liu, W. Shu, H. Luo and S. Wen, *Quantized photonic spin Hall effect in graphene*, Phys. Rev. A **95**, 013809 (2017), doi:10.1103/PhysRevA.95.013809 [preprint doi:10.48550/arXiv.1704.06045].

[8] S. Chen, X. Zhou, C. Mi, H. Luo and S. Wen, *Modified weak measurements for the detection of the photonic spin Hall effect*, Phys. Rev. A **91**, 062105 (2015), doi:10.1103/PhysRevA.91.062105.

[9] A. Aiello, N. Lindlein, C. Marquardt and G. Leuchs, *Transverse angular momentum and geometric spin Hall effect of light*, Phys. Rev. Lett. **103**, 100401 (2009), doi:10.1103/PhysRevLett.103.100401.

[10] X. Yin, Z. Ye, J. Rho, Y. Wang and X. Zhang, *Photonic spin Hall effect at metasurfaces*, Science **339**, 1405 (2013), doi:10.1126/science.1231758.

[11] P. Dong, J. Xu and J. Cheng, *Enhanced photonic spin Hall effect and its sensing application via optical Tamm state based on nanocomposites*, Phys. Plasmas **31**, 012103 (2024), doi:10.1063/5.0180207.

[12] F. Badshah, M. Abbas, Y. Zhou, H. Huang and Rahmatullah, *Coherent control of surface plasmon polaritons excitation via tunneling-induced transparency in quantum dots*, Opt. Laser Technol. **182**, 112078 (2025), doi:10.1016/j.optlastec.2024.112078.

[13] Y. Zhou, J.-W. Wang, L.-Z. Cao, G.-H. Wang, Z.-Y. Shi, D.-Y. Lü, H.-B. Huang and C.-S. Hu, *Realization of chiral two-mode Lipkin-Meshkov-Glick models via acoustics*, Rep. Prog. Phys. **87**, 100502 (2024), doi:10.1088/1361-6633/ad797d.

[14] F. Badshah, Y. Zhou, Z. Shi, H. Huang, Z. Ullah and M. Idrees, *Modulating V-type ultracold atomic tunneling via coherent injection in a mazer cavity*, Chin. J. Phys. **92**, 1674 (2024), doi:10.1016/j.cjph.2024.11.028.

[15] F. Badshah, Ammara, S. Asghar, Ziauddin and S.-H. Dong, *Investigation of diffraction grating in three-level gain medium*, Opt. Laser Technol. **177**, 111104 (2024), doi:10.1016/j.optlastec.2024.111104.

[16] F. Brennecke, S. Ritter, T. Donner and T. Esslinger, *Cavity optomechanics with a Bose-Einstein condensate*, Science **322**, 235 (2008), doi:10.1126/science.1163218 [preprint doi:10.48550/arXiv.0807.2347].

[17] M. H. Anderson, J. R. Ensher, M. R. Matthews, C. E. Wieman and E. A. Cornell, *Observation of Bose-Einstein condensation in a dilute atomic vapor*, Science **269**, 198 (1995), doi:10.1126/science.269.5221.198.

[18] K. B. Davis, M.-O. Mewes, M. R. Andrews, N. J. van Druten, D. S. Durfee, D. M. Kurn and W. Ketterle, *Bose-Einstein condensation in a gas of sodium atoms*, Phys. Rev. Lett. **75**, 3969 (1995), doi:10.1103/PhysRevLett.75.3969.

[19] F. Dalfovo, S. Giorgini, L. P. Pitaevskii and S. Stringari, *Theory of Bose-Einstein condensation in trapped gases*, Rev. Mod. Phys. **71**, 463 (1999), doi:10.1103/RevModPhys.71.463 [preprint doi:10.48550/arXiv.cond-mat/9806038].

[20] S. S. Botelho and C. A. R. Sá de Melo, *Quantum phase transition in the BCS-to-BEC evolution of p-wave Fermi gases*, J. Low Temp. Phys. **140**, 409 (2005), doi:10.1007/s10909-005-7324-3.

[21] M. Aizenman, E. H. Lieb, R. Seiringer, J. P. Solovej and J. Yngvason, *Bose-Einstein quantum phase transition in an optical lattice model*, in *Condensed matter physics and exactly soluble models*, Springer, Berlin, Heidelberg, Germany, ISBN 9783642060939 (2004), doi:10.1007/978-3-662-06390-3_23.

[22] H. Ritsch, P. Domokos, F. Brennecke and T. Esslinger, *Cold atoms in cavity-generated dynamical optical potentials*, Rev. Mod. Phys. **85**, 553 (2013), doi:10.1103/RevModPhys.85.553 [preprint doi:10.48550/arXiv.1210.0013].

[23] I. B. Mekhov, C. Maschler and H. Ritsch, *Probing quantum phases of ultracold atoms in optical lattices by transmission spectra in cavity quantum electrodynamics*, Nat. Phys. **3**, 319 (2007), doi:10.1038/nphys571 [preprint doi:10.48550/arXiv.quant-ph/0702125].

[24] K. Baumann, C. Guerlin, F. Brennecke and T. Esslinger, *Dicke quantum phase transition with a superfluid gas in an optical cavity*, Nature **464**, 1301 (2010), doi:10.1038/nature09009 [preprint doi:10.48550/arXiv.0912.3261].

[25] Y. Chen, H. Zhai and Z. Yu, *Superradiant phase transition of Fermi gases in a cavity across a Feshbach resonance*, Phys. Rev. A **91**, 021602 (2015), doi:10.1103/PhysRevA.91.021602 [preprint doi:10.48550/arXiv.1411.0429].

[26] A. Dalafi and M. H. Naderi, *Intrinsic cross-Kerr nonlinearity in an optical cavity containing an interacting Bose-Einstein condensate*, Phys. Rev. A **95**, 043601 (2017), doi:10.1103/PhysRevA.95.043601 [preprint doi:10.48550/arXiv.1701.06036].

[27] W. Chen, D. S. Goldbaum, M. Bhattacharya and P. Meystre, *Classical dynamics of the optomechanical modes of a Bose-Einstein condensate in a ring cavity*, Phys. Rev. A **81**, 053833 (2010), doi:10.1103/PhysRevA.81.053833 [preprint doi:10.48550/arXiv.1002.4437].

[28] D. Nagy, P. Domokos, A. Vukics and H. Ritsch, *Nonlinear quantum dynamics of two BEC modes dispersively coupled by an optical cavity*, Eur. Phys. J. D **55**, 659 (2009), doi:10.1140/epjd/e2009-00265-7.

[29] P. Horak and H. Ritsch, *Scaling properties of cavity-enhanced atom cooling*, Phys. Rev. A **64**, 033422 (2001), doi:10.1103/PhysRevA.64.033422 [preprint doi:10.48550/arXiv.quant-ph/0103141].

[30] C. Maschler and H. Ritsch, *Cold atom dynamics in a quantum optical lattice potential*, Phys. Rev. Lett. **95**, 260401 (2005), doi:10.1103/PhysRevLett.95.260401 [preprint doi:10.48550/arXiv.quant-ph/0508172].

[31] M. Born, E. Wolf, A. B. Bhatia, P. C. Clemmow, D. Gabor, A. R. Stokes, A. M. Taylor, P. A. Wayman and W. L. Wilcock, *Principles of optics*, Cambridge University Press, Cambridge, UK, ISBN 9780521642224 (1999), doi:10.1017/CBO9781139644181.

[32] L. Wu, H. S. Chu, W. S. Koh and E. P. Li, *Highly sensitive graphene biosensors based on surface plasmon resonance*, Opt. Express **18**, 14395 (2010), doi:10.1364/OE.18.014395.

[33] D. F. Walls and G. J. Milburn, *Quantum information*, in *Quantum optics*, Springer, Berlin, Heidelberg, Germany, ISBN 9783540285731 (2008), doi:10.1007/978-3-540-28574-8_16.

[34] F. Brennecke, T. Donner, S. Ritter, T. Bourdel, M. Köhl and T. Esslinger, *Cavity QED with a Bose-Einstein condensate*, Nature **450**, 268 (2007), doi:10.1038/nature06120 [preprint doi:10.48550/arXiv.0706.3411].

[35] Y. Colombe, T. Steinmetz, G. Dubois, F. Linke, D. Hunger and J. Reichel, *Strong atom-field coupling for Bose-Einstein condensates in an optical cavity on a chip*, Nature **450**, 272 (2007), doi:10.1038/nature06331 [preprint doi:10.48550/arXiv.0706.1390].